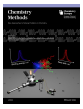

Coupling Long-Range Raman with X-Ray Photoelectron Spectroscopy for Complementary Bulk and Surface Characterization of Battery Materials

Mariusz Radtke, Karl Kopp, and Christian Hess*[a]

For the combined surface and bulk characterization of functional powder materials, we report on the direct coupling of Raman spectroscopy with X-ray photoelectron spectroscopy (XPS) within one setup, avoiding the influence of different sample states and measurement environments. Our approach is based on the Raman integration into the XPS analysis chamber, employing a long-range camera objective connected to a portable 532 nm Raman spectrometer. For optimization of the measurement geometry, a (400) single crystal (SC), chemical vaper deposition (CVD)-grown diamond was employed. The applicability of the combined XPS-Raman spectroscopy approach was first validated by measurements on powder V_2O_5, used as a commercial standard, and then demonstrated on lithium ion battery materials, that is, $Li_xV_2O_5$ lithium pentoxides. The transferability to other XPS systems is strongly facilitated by the long-range Raman-spectroscopic approach, which allowed for Raman analysis over a distance of 320 mm for the CVD-grown (400) single crystal diamond and 285 mm for $Li_xV_2O_5$. Our results demonstrate the inexpensive and straightforward implementation of coupled XPS-Raman spectroscopy for combined surface/bulk analysis.

1. Introduction

A rational design of improved functional materials strongly relies on establishing relationships between the structure of the materials and their properties/applications. The development and application of suitable techniques for structural determination therefore plays an important role in materials science. Solid-state materials are characterized by their surface and bulk properties, which can be assessed by a variety of techniques based on the use of, for example, photons, electrons, ions, and neutrons. X-ray photoelectron spectroscopy (XPS) is a unique surface technique as it allows for quantitative determination of the sample composition and chemical state analysis with a standard information depth of <10 nm. While XPS is based on the use of electrons (via the photoelectric effect), recent developments have enabled its application at elevated pressures.[1] On the other hand, Raman spectroscopy is photon-based and, if used as a vibrational technique, offers important structural information on the nature of chemical bonding and the presence of amorphous/crystalline phases, allowing for identification of solid materials.[2] Moreover, sensitivity enhancements and deeper insights into the electronic structure are feasible in selected cases, when the incident laser causes resonant electronic excitation.[3]

The combination of techniques in one setup not only decreases the time to obtain spectra, but, more importantly, avoids the influence of different sample states and measurement environments. While focusing conditions and geometric constraints typically impose restrictions on the coupling of different techniques, it should be the goal of a combined approach to gather the analysis from the same region of the solid sample. Despite considerable progress in the field, strongly triggered by developments in the context of catalytic materials, allowing, for example, for coupling of vibrational spectra with magnetic resonance, diffraction, and X-ray absorption techniques even under in situ/operando conditions by use of near-ambient pressure XPS,[4–10] reports on the combined use of Raman and XP spectroscopy have been scarce.[11,12] In the latter studies, solid samples were transferred, without exposure to air, between different chambers of one setup for Raman and XPS analysis, still leaving the state of the sample during measurement ill-defined. A combination of Raman spectroscopy with XPS has been realized by introducing vacuum-shielded optical fibers directly into the XPS measurement chamber.[13] This is justified by the limitations posed by the need of gathering the inelastically scattered light.[14,15] By using standard Raman objectives for focusing the laser, this distance is governed by the numerical aperture (NA) defined in Equation (1):[16,17]

$$NA = n\sin\theta = n\frac{D}{2f} \quad (1)$$

where n is the refractive index of the medium, D is the lens diameter, θ is the angle of incidence between the lens and the

[a] Dr. M. Radtke, K. Kopp, Prof. Dr. C. Hess
Technical University of Darmstadt
Eduard-Zintl-Institute of Inorganic and Physical Chemistry,
64287 Darmstadt (Germany)
E-mail: hess@pc.chemie.tu-darmstadt.de

Supporting information for this article is available on the WWW under https://doi.org/10.1002/cmtd.202100058

focal point, and *f* is the focal length, being used as working distance. By increasing the numerical aperture, the working distance (*f*) is being reduced, but the focal point governed by D increases. Low numerical apertures on the other hand may provide much better resolution (several μm), but the working distance also drops to a range of several micrometers.[18]

In case of Raman spectroscopy, the spot size is a factor contributing to the collection yield. Small spot sizes allow for a higher irradiation energy per area and therefore a higher Raman intensity. Regarding the coupling of XPS with Raman spectroscopy, the steric hindrance imposed by flood and ion guns makes it challenging to perform focal adjustments on such small scale within an ultra-high vacuum (UHV) chamber through the use of optical fibers and objectives. Instead of using fiber optics, another possibility is to locate the laser source outside the XPS chamber, which has the advantage that constructional changes of the XPS analysis chamber are avoided. However, the challenge in this case is the large distance between the objective and the sample, which can be resolved by specialized long-range objectives not interfering with the X-ray source. Long-range working distances of up to 80 mm are more common in Raman spectroscopy, while for distances up to 120 mm parabolic dome reflectors have been used.[15,19]

A challenge in coupling laser spectroscopy with XPS is to direct the optical and XPS foci at the same region of the sample. While XPS measures effects occur at the surface and in a depth of up to 10 nm, the Raman analysis penetrates more deeply into the material.[9,20] On the other hand, the incorporation of commercially available long-range objectives into commercial XPS systems is challenging due to reduced sampling efficiency and limited resolution, yielding, for example, for NA = 1.2 and 532 nm laser excitation a resolution of 221 nm at maximum as estimated by Equation (2):[19]

$$resolution = \frac{\lambda}{2NA} \quad (2)$$

The longest Raman working distance from the objective to the sample reported to date in specialized systems of mirrors and UHV is 120 mm.[15] Here, we present an inexpensive and straightforward approach for combined XPS and Raman spectroscopic analysis without the need for constructional changes, where the XPS and Raman foci can be adjusted separately. Raman spectra are recorded over a distance of 285 mm from the sample from outside the XPS analysis chamber, as illustrated in Figure 1A/B.

The pathway of the laser beam and its divergence were simulated by the finite difference time domain (FDTD) method and were found to be in good agreement with the experimental results (see Figure 1C). With the novel setup, powder materials with Raman cross-sections of at least 10^{-30} $cm^2 sr^{-1}$ are accessible,[21] enabling the analysis of a large variety of battery, catalytic, and sensing materials. Here, the applicability of our approach is illustrated in the context of Li-ion batteries by detailed analysis of the cathode material γ-$Li_xV_2O_5$ prior to and after electrochemistry. We also present an optimization procedure of the Raman-XPS signal adjustment based on the use of a (400) single crystal (SC) diamond, performed outside the analysis chamber.

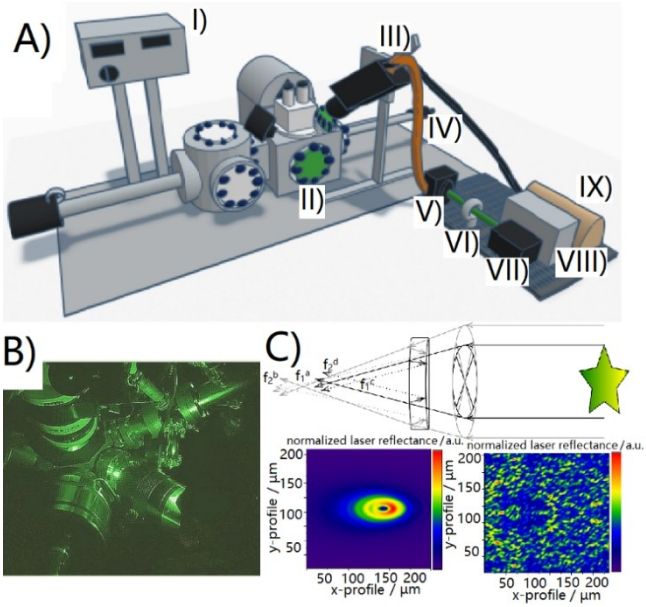

Figure 1. A) Schematics of the combined XPS-Raman setup based on long-range Raman measurements comprised of: I – Hardware control, II – XPS chamber, III – Raman probe head with laser-focusing camera objective, IV – optical excitation/signal collection fibers, V – optics laser entrance, VI – laser focusing lens, VII – solid-state laser, VIII – Peltier chiller, IX – Raman spectrometer. B) The combined XPS-Raman setup in use. C) Finite difference time domain simulations of the laser spot on the sample surface for 532 nm excitation, a distance of 285 mm, and a 33 mm lens (left), as well as for a casual 0.5x magnification, 532 nm excitation, and 285 mm distance (right). The bimodal laser spot is a combination of the double-objective lens and the incident angle, which results in two focal points f_2^d and f_1^a. Images of the experimental laser spots resemble the simulated bimodal distribution (see Figure 2).

2. Results and Discussion

2.1. Optical Considerations and Simulations of the XPS-Raman Spectroscopy Setup

Media of various refractive indices influence the divergence of the laser light along its path to the sample and back. In the present case shown in Figure 1, the laser beam emitted by the probe-head (III) is focused by the camera objective into the XPS-chamber under UHV (10^{-8} mbar). Thereby, the laser beam travels from the source (VII) to the Raman beam-splitting system (III) and then changes the medium from air to the XPS-flange borosilicate glass and finally to vacuum when entering the analysis chamber. Figure 1C shows results of FDTD simulations of the Maxwell equations describing the 532 nm laser beam in a distance of 285 mm from the lens (at the end of III) to the sample at an angle of incidence of 35°.

The divergence of the laser beam is governed by the lens (diameter: 33 mm), which matches the size of the XPS window. Similar approaches based on camera objectives have also been employed by others under ambient pressure conditions and by

using a reflection chamber.[15] Here, we make use of the ultra-high vacuum within the XPS analysis chamber. The difference between two media of various refractive indices, air outside the XPS chamber and vacuum inside, allows for gathering a less distorted Raman signal.[25] We did not observe any significant influence of the varying refractive index on the laser divergence in our simulations.

The simulations considered two refractive indices, that is, that of the air outside the chamber, and that of the vacuum within the chamber. The presence of a borosilicate window in the XPS-flange causes additional deflection of the beam, as illustrated in Figure 1C, and adds to signal loss. The second simulation, based on a casual long-range objective (0.5x, NA = 0.02) shows the expected result, that is, the failure of focusing the laser beam in one spot due to the angle of incidence. In addition, the intensity of the scattered laser light is significantly lower as compared to the focus conditions present in our setup.

As an example, Figure 2A shows the experimental result of the laser beam focused at an angle of 35°, exhibiting a similar bimodal distribution as predicted by the FDTD simulations. In addition, the order of magnitude of the sizes of laser spots in the simulations showed similar trends to those measured in experiment. The spot size of roughly 500 μm necessitates using higher laser powers of up to 35 mW, as the intensity for such a large spot will be about 100 times than that of common Raman microscopes using typical spot sizes of a few μm.

One of the characteristics of our measurement system is the difference in environments. The laser passes through media of various refractive indices. The scattered light comes into contact with the camera objective by passing through the glass-protected flange, allowing a transmission of 80% and up to 550 nm as shown in Figures 1B and C. At this incident point, which is most probably responsible for the majority of intensity loss in the Raman spectrum, we were able to obtain a spectrum matching that of silicon dioxide. This might be the source of the observed fluorescence background, which was subtracted from Figure 2 for clarity. The raw spectrum is included in the Supporting Information (see Figure S2).

We note that more focused collection of the scattered light by reduced laser divergence could lead to higher signal yields. Laser divergence could be improved by signal collimation according to Equation (3):

$$\theta = \arctan\left(\frac{D_f - D_i}{2l}\right) \tag{3}$$

where θ stands for the divergence. D_f and D_i are the beam diameters outside the focal points and l is the distance between those points. Additionally, it is possible to narrow the focal laser spot to smaller values and therefore to reach higher Raman intensities by changing the distance between the flange and lens (with simultaneous variation of the focal points f_1 and f_2), as shown in Figure 1, according to the principle of the lens equation.

Nevertheless, placing the detector for the scattered light outside the XPS chamber and thus making it independent from the height (z-)adjustment of the sample enables us to differentiate between the XPS and the Raman focus. The Raman focus was optimized by changing the focal distance directly on the camera objective, whereas the XPS focus was adjusted by the standard z-screw.

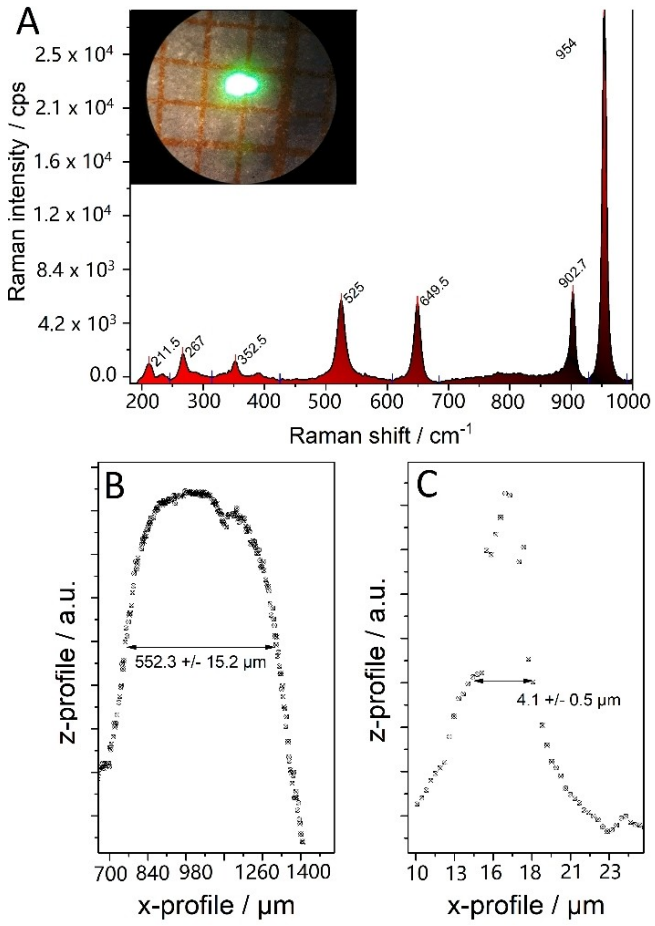

Figure 2. A) Raman spectrum of of γ-$Li_xV_2O_5$ recorded over a 285 mm distance and at an angle of 35°. The inset shows a picture of the laser spot inside the analysis chamber. B) Profile of the long-distance laser spot. C) Profile of a laser spot in conventional Raman microscopy. For details, see main text.

2.2. Material Requirements for Applicability

The size of the material under investigation was in the range of several hundreds of micrometers, matching the size of the spot achieved by the 35°-tilted laser beam depicted in Figure 2. If the size of the material is considerably smaller, for example, several micrometers, the recording of long-distance Raman spectra becomes a challenge due to the decreased intensity of the incident radiation. This limitation may be overcome by the use of a laser source with higher power. In our experiments, we set the laser power to 35 mW, which may be detrimental at short distance, but did not lead to any laser-induced effects of the sample due to the large reduction in laser intensity (see also above). An example of such a Raman spectrum of γ-$Li_xV_2O_5$ is shown in Figure 2A. The corresponding XPS spectra from the

combined experiment are presented in Figure 4 and will be discussed below. The Raman-active modes of γ-$Li_xV_2O_5$ were elucidated from a standard symmetry adapted linear combination (SALC) approach, in good agreement with the literature.[22,26]

To further specify the aspects relevant to the recording of long-distance Raman spectra, we have performed a series of measurements as a function of the geometry of incidence (see also below). Regarding the spot size, we found a dependence of the incidence angle on the shape and on the spot diameter. For example, at 35°, we found the spot size to be 552.3 ± 15.2 μm, approximately matching the size of the particles in the cathode material. Based on our results, we postulate that the applicability of long-distance Raman spectroscopy is facilitated by matching the measurement spot size with a homogenously composed piece of material. Established strategies to transform the size of a material and improve the homogenization are ball-milling, ultrasonication, and focused ion beam (FIB)-induced transformation. Please note that all these techniques require pure conditions and bear a jeopardy of cross contamination (FIB: foreign ions, for example, Cr; ball milling: Fe compounds; ultrasonication: incorporation of Ti).[27–29] An influence of the spot size on sample properties was not observed in conventional short-range Raman measurements, which were performed as a control (see Figure 2).

The S/N ratio of the spectrometer readout of the long-distance measurements (285 mm, diameter: 552.3 ± 15.2 μm) compared to standard Raman measurements (spot diameter: 4.1 ± 0.5 μm) decreased by a factor of 10, which was confirmed by utilizing the same laser power and acquisition time for the material in focus, that is, γ-$Li_xV_2O_5$ and (400)-CVD grown SC diamond. The S/N ratio was established by consecutive acquisition of three spectra and dividing the band intensity by the mean of the band intensity over three measurements.[30] The lower S/N ratio in the long-distance measurements is caused by the relatively large laser spot as verified by experiment (see Figure 2). The laser fluence on a spot of the same size (552.3 μm) was estimated outside the XPS chamber under ambient conditions and was found to be 1461 W cm^{-2}.

In order to assess the sensitivity of the setup, the Raman signals were compared with literature values reported for SC CVD diamond (100) (see Table S1).[31] We note that our reference was the (400) synthetic diamond. The following analysis was based on ratios of areas under the Raman bands under standardized conditions described in the Materials and Methods section. The V_2O_5 reference was found to scatter 1.1x better than the (400) SC diamond, while γ-$Li_xV_2O_5$ scattered the laser even 1.6x better than CVD SC diamond under the same long-range measurement conditions.

2.3. Optimization of the XPS-Raman Spectroscopy Setup

In order to characterize our setup regarding the influence of the incidence angle of the laser, we have chosen a high-quality diamond standard, that is, (400)-CVD grown SC diamond, which shows a Raman band at 1332 cm^{-1} due to the ubiquitous sp^3-hybridized carbon atoms, respectively; FWHM values range within 2–10 cm^{-1} in the conventional and long-distance Raman spectra, depending on the diamond type (CVD- or HPHT-grown).[32]

The results of angle-dependent measurements are shown in Figure 3. For flexibility, the measurements were performed outside the XPS analysis chamber, allowing to use a wide range of angles in several geometries. In the upright geometry, the beam was directly reflected back to the spectrometer, corresponding to an angle of incidence of 90°.

Once the distance from the focal point was increased, the intensity of the D band dropped monotonically. Please note that the intensity of the D band was normalized by the intensity at 220 mm distance from the sample where the intensity was the highest. We observed a dependence of the incidence angle on Raman intensity, where an angle of 15° turned out to yield a higher intensity than 10° at the same distance. We relate these observations to the presence of the bimodal laser spot distribution shown in Figure 1, which possibly generates two Raman hot spots that contribute synergistically to the gathered signal. We have also performed the measurements of the full width at half maximum (FWHM), which was found to increase with the distance from the source. This behavior may be explained by spectral diffusion, a well-known phenomenon in

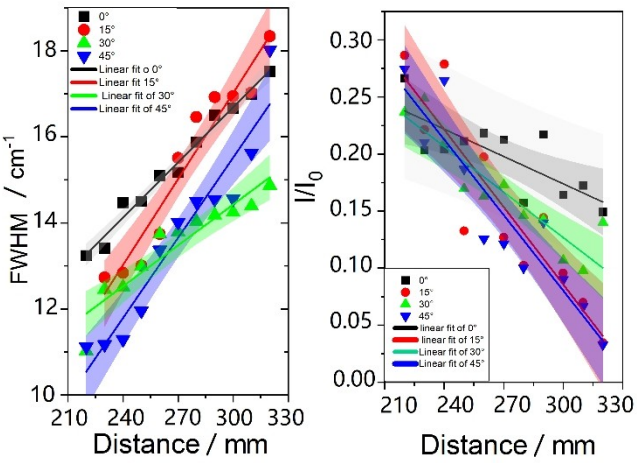

Figure 3. Comparison of the geometries of laser incidence on the sample based on measurements of the Raman D-band of (400)-CVD grown SC diamond outside the ultrahigh vacuum chamber with fitted 95% confidence intervals. The intensity I_0 refers to the D-band intensity at 1332 cm^{-1} at 90° incidence. We note the fact that the root-mean square roughness (rms) of the sample will have an influence on the incidence and reflection angle of the laser/Raman signal. In case of the diamond sample, the rms was estimated to be less than 1 nm. Therefore this statement corresponds to materials where the grain size reaches the same order as the Abbé limit (meaning roughly 200 nm).[33]

Table 1. Results from the combined XPS-Raman spectroscopy analysis of V_2O_5 (standard) and γ-$Li_xV_2O_5$ electrode samples.

Signals	$[V^{5+}]$/[%]	$[V^{3+/4+}]$/[%]	[V=O]/[cm^{-1}]
γ-$Li_xV_2O_5$	85.1	14.9	953.8
ε-$Li_xV_2O_5$	93.8	6.2	995.5
V_2O_5	93.4	6.6	994.9

long-distance Raman measurements.[34] It stands to reason that the target geometry is associated with the highest intensity and lowest FWHM, which according to Figure 3, at a distance of 285 mm, is obtained for incidence angles of 30° and 45°.

2.4. Application of the XPS-Raman Setup to Battery Materials

Prior to applications, we validated the use of the novel XPS-Raman setup by experiments on commercial V_2O_5, the separate XP and Raman spectra of which are well documented in the literature.[35,36] While V_2O_5, in the current context, is mainly employed as a methodical/spectroscopic standard, it has been widely applied, for example in electrochemistry, heterogeneous catalysis, and gas sensing.[37] In order to investigate the potential of the coupling between XP and long-distance Raman spectroscopy for applications in the context of Li-ion batteries, we performed a series of measurements on γ-$Li_xV_2O_5$-based cathode materials, comparing their state prior to charging (reference) to that after charging. To this end, γ-$Li_xV_2O_5$ was charged up to 4.87 V versus Li/Li^+ in a two-electrode combination (see Figure 4A), while the reference state of γ-$Li_xV_2O_5$ was left uncharged and without electrolyte contact. The results from the combined XPS-Raman measurements are summarized in Tables 1 and 2 and Figure 4 and will be discussed in the following. Additional data is provided in the Supporting Information.

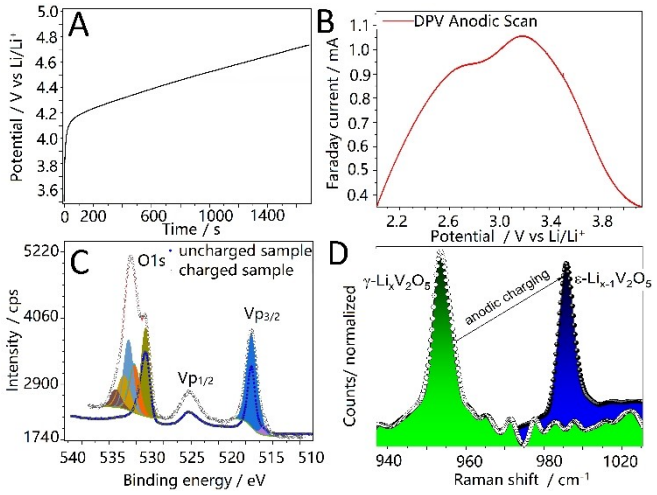

Figure 4. Electrochemical and spectroscopic data of $Li_xV_2O_5$ recorded by the combined XP-Raman spectroscopy setup. A) Chronopotentiometric curves of 2 μA charging over time. B) Differential pulse voltammograms showing the redox activity of the sample. C) XPS O 1s and V 2p photoemissions together with the results of a fit analysis. D) Long-distance Raman bands showing the symmetric stretching mode of vanadium oxide (normalized to the V=O intensity in V_2O_5). For details, see the main text.

Table 2. Results from the XPS analysis of the surface composition of $Li_xV_2O_5$ prior to and after charging.

Sample/signal	C [at.%]	O [at.%]	P [at.%]	V [at.%]
$Li_xV_2O_5$	30.8	44.7	–	12.1
$Li_xV_2O_5$ charged	26.1	29.7	4.9	5.0
Sample/signal	**Li [at.%]**	**N [at.%]**	**F [at.%]**	
$Li_xV_2O_5$	9.8	1.8	–	
$Li_xV_2O_5$ charged	10.3	0.6	23.4	

The reference sample V_2O_5 was used to validate the novel XP-Raman spectroscopy setup. The obtained XPS and Raman results (see Table 2 and the Supporting Information) are fully consistent with data from our own separate measurements as well as that from the literature.[22,38,39] In particular, the characteristic Raman signature of V_2O_5 is detected, including the stretching vibration of vanadyl (V=O) at 995 cm^{-1}.[40] In contrast, highly lithiated γ-$Li_xV_2O_5$ shows a red-shifted V=O stretch (A_{1g} mode) at 953 cm^{-1},[22] highlighting the sensitivity of this mode to structural changes. Note that the position of the vanadyl feature was unbiased by the presence of the Al_2O_3 substrate for the cathode material.

The electrochemical measurements on the γ-$Li_xV_2O_5$ show two distinct peaks responsible for the vanadium activity, as proven by differential pulse voltammetry (DPV, see Figure 4B).[41] The lack of binder did not affect the electrochemical measurements, which yielded results expected from the literature.[42] The anodic peak at 3.15 V versus Li/Li^+ corresponds to the γ-ε phase transformation upon lithium exertion from $Li_xV_2O_5$ and the anodic peak at 3.4 V versus Li/Li^+ to the V^{4+} to V^{5+} oxidation due to electron stripping.[43] In the course of the potentiostatic measurement shown in Figure 4A, the Li^+ was exerted from the γ-$Li_xV_2O_5$ bi-layered structure and the Raman spectrum was slowly moving towards a V_2O_5 state. This was observed as a blue-shift of the vanadyl stretching mode (see Figure 4D). However, upon Li^+ de-intercalation, the sample did not adopt the pure V_2O_5 state but rather underwent a polymorphic transformation from γ-$Li_xV_2O_5$ to ε-$Li_xV_2O_5$, that is, the Li-impoverished polytype of $Li_xV_2O_5$.

As vanadium pentoxide has a layered structure, the V=O functionalities may be arranged inwards or backwards.[44] In case of the lithiated structure, the V=O groups of two sheets share the lithium ion in coordination,[45] while, upon loosing Li^+, the structure reverses its tilted conformation as it transforms from the γ to the ε polymorph. As a result of the phase change, the Raman spectra are characterized by a blue shift from 954 to 996 cm^{-1} (see Table 1). While charging of $Li_xV_2O_5$ leads to distinct changes of the V_2O_5 bulk structure, surface analysis by XPS reveals only minor variations of the vanadium oxidation states. However, as the applied potential during charging is at the borderline of electrolyte stability, electrolyte decomposition and thus reaction with the $Li_xV_2O_5$ sample becomes feasible, which have been discussed in the context of cathode-electrolyte interphase (CEI) formation.[46] An additional effect supporting the formation of CEI is the ability of the electrolyte (ethylene carbonate) to create metastable complexes with lithium.[45,47]

Table 2 contains the surface composition based on the XPS analysis prior to and after charging of γ-$Li_xV_2O_5$. As expected, the uncharged material exhibits mainly C, O, V, and Li. The Li/V ratio of 0.8 suggests a Li surface content x in γ-$Li_xV_2O_5$ of 1.62; on the other hand, the V 2p analysis indicates surface vanadium oxidation as compared to the bulk (see Table 1). Interestingly, the XP spectra of charged γ-$Li_xV_2O_5$ show clear differences,

resulting from the exposure to the electrolyte and the electrochemical treatment.

As charging was performed in a Li-containing electrolyte (see Supporting Information; 1 M $LiPF_6$ in 1:1 EC:DMC) under an inert atmosphere, additional P and F signals are expected (see Table 2).[47] In fact, detailed analysis of the F 1s photoemission reveals contributions at 685.0 and 687.3 eV, consistent with the presence of LiF and lithium fluorophosphates ($Li_xPF_yO_z$), respectively, resulting from $LiPF_6$ salt decomposition.[47]

This is supported by the P 1 s signal at 135.7 eV, significantly red-shifted in comparison to $LiPF_6$, and the Li 1 s photoemissions at 55.7 eV (LiF) and 57.0 eV ($Li_xPF_yO_z$).[47] In combination with the convolution of the O 1s peak, yielding a high-energy contribution due to $Li_xPF_yO_z$ at 533.8 eV, the stoichiometry of the formed lithium fluorophosphates can be estimated as $x = 0.7$, $y = 3.1$, and $z = 0.4$. Further analysis of the O 1s photoemission reveals additional contributions at 530.2, 531.6, 532, and 532.8 eV, which – consistent with the V 2p and C 1s signals – can be attributed to vanadium oxide, C=O, OH/water, and C–O, respectively (see Supporting Information). The carbon- bonded oxygen signals are better discussed on the basis of the corresponding C 1s photoemissions at 285.8, 286.7, and 288.7 eV, which are typical for C–O, O–C–O, and O–C=O functionalities[48] and can be associated with alcohol, ethers, and carbonates, respectively.[49] We note that the presence of carbon species results from the decomposition of electrolyte components, that is, ethylene carbonate (EC) and dimethyl carbonate (DMC), upon charging. A further high-energy peak at 290.7 eV has previously been assigned to C–F, originating from the reaction of carbonates with HF (formed from PF_6^- hydrolysis).[49] Thus, from the XPS analysis, we can conclude that charging at potentials exceeding 4.8 V leads to electrolyte decomposition/reaction resulting in the formation of inorganic compounds (LiF, $Li_xPF_yO_z$) and polycarbonates as part of a solid electrolyte interphase (CEI) layer, in agreement with previous studies on other cathode materials for lithium-ion batteries.[47,49,50]

As demonstrated above, the combination of Raman and XP spectroscopy provides a unique possibility for both surface (photoelectrons) and bulk (phonon) analysis of functional materials. We employed green laser excitation, which penetrates the XPS-machine shielding glass (Figure 1A), yielding, as a compromise, a signal with some fluorescence background. By the combined XP-Raman spectroscopy analysis, the electrode-electrolyte interaction has been elucidated in detail. Besides the potential-dependent polymorphization, as evidenced by the Raman spectra in Figure 4D, the decomposition of electrolyte has been accessible by XPS surface analysis as shown in Figure 4C and Tables 1/2. Owing to its potential for the characterization of energy storage materials, further optimization towards in situ/operando XP-Raman spectroscopy with electrochemistry would be desired in the future in order to monitor the potential-dependent changes directly.

3. Conclusion

In this contribution, we demonstrated the successful coupling of XP and Raman spectroscopy by combining a long-distance Raman approach with a conventional XPS analysis chamber. We studied several geometries of the XP-Raman spectroscopy setup and found a distance of 285 mm and an angle of incidence of 45° to show the best signal-to-noise ratio. Our approach is based on a standard camera objective and a commercial Raman spectrometer equipped with a 532 nm excitation laser, facilitating transferability to other instruments. The Raman spot size of about 550 μm matched the XPS sampling diameter of 250–1000 μm, enabling analysis from the same sample area within the XPS analysis chamber, thus avoiding the influence of different environments. The XP-Raman spectroscopy approach was first validated using commercial V_2O_5 powder as a reference compound and then applied to lithium-ion battery materials. Comparison of different charging states of γ-$Li_xV_2O_5$/graphite clearly demonstrated the complementary nature of Raman and XP spectra. While Raman spectroscopy provided structural details, in particular, on the polymorphization of γ-$Li_xV_2O_5$ to lithium-poor ε-$Li_xV_2O_5$, XPS analyses revealed the quantitative surface composition. Combining these findings allows to gain detailed insight into the potential-dependent phase transformations and cathode-electrolyte interactions, including CEI formation. Further developments of this combined surface/bulk analysis may include in situ/operando measurements of in-chamber batteries as well as its application in other areas of research.

Experimental Section

V_2O_5 (Alfa Aesar, UK, 99.9% purity) was used as a standard material for all Raman and XP spectroscopic comparisons and as a reference. γ-$Li_xV_2O_5$ was synthesized according to the procedure described elsewhere.[22] Briefly, 250 mg of lithium carbonate (Sigma Aldrich, Germany, 99.9% purity) and 250 mg of vanadium(V) oxide (Alfa Aesar, UK, 99.9% purity) were added into a two-neck flask charged with a magnetic stirrer and equipped with a reflux condenser and pressure-regulated dropping funnel. The material was brought to reflux, and 3 mL of 20% aqueous trisodium ascorbate trihydrate (Sigma Aldrich, Germany 99.9% purity) was added into the refluxing mixture, which immediately turned pale yellow. The precipitate was collected by vacuum filtration, dried overnight at 80 °C and annealed in an oven at 400 °C (heating rate 5 °C min^{-1}, annealing period 2 h and cooling rate 5 °C min^{-1}). The orange precipitate was collected and characterized by Raman spectroscopy, XPS, and XRD. Raman spectra confirmed the presence of lithium vanadium pentoxide stretching vibrations and matched the literature for γ-$Li_xV_2O_5$.

Raman spectra were recorded on a Kaiser Optical spectrometer equipped with a Peltier-cooled CCD camera and a Cobolt laser (Hübner Photonics) with 532 nm laser excitation. The Raman spectrometer was calibrated using an argon lamp. All in-chamber Raman spectra were calibrated on a (400) CVD-grown single-crystal (SC) diamond, synthesized according to the procedure described elsewhere.[23,24] The laser power was varied as detailed in the following: ex-chamber measurements of $Li_xV_2O_5$ and V_2O_5, as well as of all starting materials for the synthesis, were recorded at 2.3 mW power with the laser spot size varying, depending on sample

roughness, but always in the range of 5 μm. For the in-chamber measurements, the laser power was increased to 35 mW and the radiation was focused onto the sample with the help of a Raman probe-head (Kaiser Optical, USA) equipped with a standard commercial 100x Canon camera objective (F5.6). The laser spot size was measured with a digital microscope (Zeiss, Germany) and standard millimetre paper (DIN 476-2:2008-02) and was found to be in the range of 500 μm. Raman spectra were collected in upright and tilted configuration over the glass-shielded vacuum flanges of the analysis chamber of the XP spectrometer, as will be described in more detail below. The electrolyte was LP30 (1 M $LiPF_6$ in 1:1 dimethylcarbonate (DMC): ethylene carbonate (EC), purchased from Alfa Aesar, UK).

XP spectra were recorded on a SSX100 ESCA Spectrometer from Surface Science Laboratories Inc. equipped with a monochromatic $Al_{K\alpha}$ source (9 kV, 10 mA). The measurement spot diameter was 250–1000 μm. Survey spectra were acquired with a pass energy of 150 eV, a resolution of 0.16 eV, and a rate of 0.5 $eV\,s^{-1}$. For detailed spectra, a pass energy of 50 eV, a resolution of 0.1 eV, and rate of 0.1 $eV\,s^{-1}$ were employed. The XP spectrometer was calibrated using Au foils and the respective position of the Au $4f_{7/2}$ emission at an analyser position of 35° with respect to the X-ray incidence on the sample. XP spectra were fitted and analysed using CASA XPS (version 2.3.22PR1.0). Data analysis included subtraction of a Shirley background and a peak-fit analysis. Peak fitting was performed with Casa XPS using 70/30 Gaussian-Lorentzian product functions. Atomic ratios were determined from the integral intensities of the signals, which are corrected by empirically derived sensitivity factors.

For combined XP-Raman spectroscopy analysis the material was pressed on an Al_2O_3 mesh and inserted into the XPS analysis chamber with a base pressure of $2\cdot10^{-8}$ mbar and equipped with standard vacuum viewport windows (see Figure 1).

Electrochemical charging was performed in an in situ cell (EL-cell GmbH, Hamburg, Germany) with Li as an anode (thickness: 0.5 inch, Alfa Aesar, U.K.) and LP30 as electrolyte (1 M $LiPF_6$ solution in 1:1 dimethyl carbonate: ethylene carbonate, Alfa Aesar, U.K.), by applying a 2 μA current up to 4.8 V versus Li/Li^+ and staying at this potential for 10 h.

The finite difference time domain (FDTD) simulations of the laser beam were performed with the help of the Maxwell-equation solver implemented in the Lumerical 2021 software optimized for a wavelength of 532 nm and incidence angles of 10–45°.

Acknowledgements

This research was funded by Deutsche Forschungsgemeinschaft (DFG) grant number: DFG, HA 6128/6-1.

Conflict of Interest

The authors declare no conflict of interest.

Keywords: combined surface/bulk analysis · lithium-ion batteries · lithium vanadium oxide · Raman spectroscopy · XPS

[1] E. A. Carbonio, J.-J. Velasco-Velez, R. Schlögl, A. Knop-Gericke, *J. Electrochem. Soc.* **2020**, *167*, 5, 054509.
[2] K. Hashimoto, V. R. Badarla, A. Kawai, T. Ideguchi, *Nat. Commun.* **2019**, *1*, 4411.
[3] C. G. Kontoyannis, N. V. Vagenas, *Analyst* **2000**, *125*, 251.
[4] S. J. Tinnemans, J. G. Mesu, K. Kervinen, T. Visser, T. A. Nijhuis, A. M. Beale, D. E. Keller, A. M. van der Eerden, B. M. Weckhuysen, *Catal. Today* **2006**, *113*, 3.
[5] V. M. V. G. Nageswaran, *Front. Chem.* **2020**, *8*, 620557.
[6] S. Han, D. Zhao, T. Otroshchenko, H. Lund, U. Bentrup, V. A. Kondratenko, N. Rockstroh, S. Bartling, D. E. Doronkin, J.-D. Grunwaldt, U. Rodemerck, D. Linke, M. Gao, G. Jiang, E. V. Kondratenko, *ACS Catal.* **2020**, *10*, 8933.
[7] A. Brückner, E. Kondratenko, *Catal. Today* **2006**, *113*, 16.
[8] A. Indra, P. W. Menezes, K. Kailasam, D. Hollmann, M. Schröder, A. Thomas, A. Brückner, M. Driess, *Chem. Commun.* **2016**, *52*, 104.
[9] C. Hess, *Chem. Soc. Rev.* **2021**, *50*, 3519.
[10] A. R. Head, O. Karslıoglu, T. Gerber, Y. Yu, L. Trotochaud, J. Raso, P. Kerger, H. Bluhm, *Surf. Sci.* **2017**, *665*, 51.
[11] C.-T. Nottbohm, C. Hess, *Catal. Commun.* **2021**, *22*, 119822.
[12] C. Hess, *Top. Catal.* **2013**, *56*, 1593.
[13] A. Shavorskiy, S. Neppl, D. S. Slaughter, J. P. Cryan, K. R. Siefermann, F. Weise, M.-F. Lin, C. Bacellar, M. P. Ziemkiewicz, I. Zegkinoglou, M. W. Fraund, C. Khurmi, M. P. Hertlein, T. W. Wright, N. Huse, R. W. Schoenlein, T. Tyliszczak, G. Coslovich, J. Robinson, R. A. Kaindl, B. S. Rude, A. Ölsner, S. Mähl, H. Bluhm, O. Gessner, *Rev. Sci. Instrum.* **2014**, *85*, 093102.
[14] J. Steidtner, B. Pettinger, *Rev. Sci. Instrum.* **2007**, *78*, 103104.
[15] Y. Tian, J. W. Su, J. Ju, Q. Liu, *Biomed. Opt. Expr.* **2017**, *8*, 5243.
[16] D. Cialla-May, M. Schmitt, J. Popp, *Phys. Sci. Rev.* **2019**, *4*, 1.
[17] M. Kang, Y. Ra'di, D. Farfan, A. Alù, *Phys. Rev. Appl.* **2020**, *13*, 044016.
[18] A. K. Singh, S. A. Khan, Z. Fan, T. Demeritte, D. Senapati, R. Kanchanapally, P. C. Ray, *J. Am. Chem. Soc.* **2012**, *134*, 8662.
[19] A. Downes, *Appl. Spectrosc. Rev.* **2019**, *54*, 445.
[20] M. O. Guerrero-Pérez, M. A. Bañares, *Catal. Today* **2006**, *113*, 48.
[21] L. G. Cançado, A. Jorio, M. A. Pimenta, *Phys. Rev. B* **2007**, *76*, 064304.
[22] R. Baddour-Hadjean, E. Raekelboom, J. P. Pereira-Ramos, *Chem. Mater.* **2006**, *18*, 3548.
[23] M. Radtke, A. Slablab, S. Van Vlierberghe, C.-N. Lin, Y.-J. Lu, C.-X. Shan, *J. Carbon Res.* **2020**, *6*, 37.
[24] Y.-C. Chen, Y.-J. Lu, C.-N. Lin, Y.-Z. Tian, C.-J. Gao, L. Dong, C.-X. Shan, *J. Mater. Chem. C* **2018**, *6*, 5727.
[25] M. N. M. N. Perera, W. E. K. Gibbs, S. Juodkazis, P. R. Stoddart, *J. Raman Spectrosc.* **2017**, *48*, 1182.
[26] G. T. Went, S. T. Oyama, A. T. Bell, *JPC* **1990**, *94*, 4240.
[27] J. Lim, S.-H. Kim, R. Aymerich Armengol, O. Kasian, P.-P. Choi, L. T. Stephenson, B. Gault, C. Scheu, *Angew. Chem. Int. Ed.* **2020**, *59*, 5651.
[28] J. Liu, R. Niu, J. Gu, M. Cabral, M. Song, X. Liao, *Sci. Rep.* **2020**, *10*, 10324.
[29] S. Ali, K. Mourad, G. Abdurahim, *Ceram. Int.* **2015**, *41*, 1121.
[30] X.-G. Fan, Y. Zeng, Y.-L. Zhi, T. Nie, Y.-j. Xu, X. Wang, *J. Raman Spectrosc.* **2021**, *52*, 890.
[31] K. Srimongkon, S. Ohmagari, Y. Kato, V. Amornkitbamrung, S. Ichishikata, *Diamond Relat. Mater.* **2016**, *63*, 21.
[32] R. S. Krishnan, *Nature* **1945**, *155*, 171.
[33] M.-L. Lin, Y.-C. Leng, X. Cong, D. Meng, J. Wang, X.-L. Li, B. Yu, X.-L. Liu, X.-F. Yu, P.-H. Tan, *Sci. Bull.* **2020**, *65*, 1894.
[34] P. Finnie, J. Ouyang, J. Lefebvre, *Sci. Rep.* **2020**, *10*, 9172.
[35] F. Ureña-Begara, A. Crunteanu, J.-P. Raskin, *Appl. Surf. Sci.* **2017**, *403*, 717.
[36] P. Shvets, O. Dikaya, K. Maksimova, A. Goikhman, *J. Raman Spectrosc.* **2019**, *50*, 1226.
[37] S. Sharma, M. Madou, *Phil. Trans. R. Soc. A: Mat., Phys. Eng. Sci.* **2012**, *370*, 2448.
[38] J. Mendialdua, R. Casanova, Y. Barbaux, *J. Electron Spectrosc. Relat. Phenom.* **1995**, *71*, 249.
[39] M. Radtke, C. Hess, *Molecules* **2021**, *26*, 4667.
[40] I. E. Wachs, *Dalton Trans.* **2013**, *42*, 11762.
[41] Y.-R. Lu, T.-Z. Wu, C.-L. Chen, D.-H. Wei, J.-L. Chen, W.-C. Chou, C.-L. Dong, *Nanoscale Res. Lett.* **2015**, *10*, 387.
[42] D. Wei, M. R. J. Scherer, C. Bower, P. Andrew, T. Ryhänen, U. Steiner, *Nano Lett.* **2012**, *12*, 1857.
[43] D. W. Murphy, P. A. Christian, F. J. DiSalvo, J. V. Waszczak, *Inorg. Chem.* **1979**, *18*, 2800.
[44] L. R. De Jesus, G. A. Horrocks, Y. Liang, A. Parija, C. Jaye, L. Wangoh, J. Wang, D. A. Fischer, L. F. J. Piper, D. Prendergast, S. Banerjee, *Nat. Commun.* **2016**, *7*, 12022.

[45] J. S. Braithwaite, C. R. A. Catlow, J. D. Gale, J. H. Harding, *Chem. Mater.* **1999**, *11*, 4052.
[46] Y. Wu, X. Liu, L. Wang, X. Feng, D. Ren, Y. Li, X. Rui, Y. Wang, X. Han, G.-L. Xu, H. Wang, L. Lu, X. He, K. Amine, M. Ouyang, *En. Stor. Mat.* **2021**, *37*, 77.
[47] Y. Yu, P. Karayaylali, Y. Katayama, L. Giordano, M. Gauthier, F. Maglia, R. Jung, I. Lund, Y. Shao-Horn, *J. Phys. Chem. C* **2018**, *122*, 27368.
[48] J. Moulder, J. Chastain, *Handbook of X-ray Photoelectron Spectroscopy: A Reference Book of Standard Spectra for Identification and Interpretation of XPS Data*, Physical Electronics Division, Perkin-Elmer Corporation, **1992**, ISBN: 0962702625.
[49] I. Azcarate, W. Yin, C. Méthivier, F. Ribot, C. Laberty-Robert, A. Grimaud, *J. Electrochem. Soc.* **2020**, *167*, 080530.
[50] S. Fang, D. Jackson, M. L. Dreibelbis, T. F. Kuech, R. J. Hamers, *J. Power Sources* **2018**, *373*, 184.

Manuscript received: June 22, 2021
Version of record online: September 20, 2021